Magnetic Inflation and Stellar Mass. V. Intensification and Saturation of M-dwarf Absorption Lines with Rossby Number

Philip S. Muirhead[1] [iD], Mark J. Veyette[1] [iD], Elisabeth R. Newton[2] [iD], Christopher A. Theissen[3,5] [iD], and Andrew W. Mann[4] [iD]
[1] Department of Astronomy, Institute for Astrophysical Research, Boston University, 725 Commonwealth Avenue, Boston, MA 02215, USA; philipm@bu.edu
[2] Department of Physics & Astronomy, Dartmouth College, Hanover, NH 03755, USA
[3] Center for Astrophysics and Space Sciences, University of California, San Diego, 9500 Gilman Drive, La Jolla, CA 92093, USA
[4] Department of Physics and Astronomy, University of North Carolina at Chapel Hill, Chapel Hill, NC 27599, USA
Received 2019 September 24; revised 2019 November 25; accepted 2019 November 26; published 2020 January 16

Abstract

In young Sun-like stars and field M-dwarf stars, chromospheric and coronal magnetic activity indicators such as Hα, X-ray, and radio emission are known to saturate with low Rossby number (Ro ≲ 0.1), defined as the ratio of rotation period to convective turnover time. The mechanism for the saturation is unclear. In this paper, we use photospheric Ti I and Ca I absorption lines in the Y band to investigate magnetic field strength in M dwarfs for Rossby numbers between 0.01 and 1.0. The equivalent widths of the lines are magnetically enhanced by photospheric spots, a global field, or a combination of the two. The equivalent widths behave qualitatively similar to the chromospheric and coronal indicators: we see increasing equivalent widths (increasing absorption) with decreasing Ro and saturation of the equivalent widths for Ro ≲ 0.1. The majority of M dwarfs in this study are fully convective. The results add to mounting evidence that the magnetic saturation mechanism occurs at or beneath the stellar photosphere.

1. Introduction

Magnetic activity of low-mass stars, specifically M-dwarf stars, is of significant interest to multiple areas of astrophysics. Magnetized winds are expected to be the dominant rotational breaking mechanism in main-sequence M-dwarf stars (e.g., Bouvier et al. 2014) as well as the dominant orbital breaking mechanism in post-common envelope binary stars (e.g., Muirhead et al. 2013) and cataclysmic variable stars (e.g., Skinner 2014), both of which often contain M-dwarf stars. Magnetic heating of M-dwarf chromospheres and coronae results in high-energy radiation (e.g., France et al. 2016; Stelzer et al. 2016) and likely also coronal mass ejections (e.g., Kay et al. 2016), all of which have implications for the atmospheres and surfaces of orbiting extrasolar planets.

Magnetic activity, broadly defined, is commonly probed using a handful of observational signatures, mostly through its effects on the stellar upper atmosphere. The equivalent widths of Hα or Ca II emission lines are common tracers for magnetic activity, originating in the chromospheres of stars, as they do in the Sun (e.g., Noyes et al. 1984; Soderblom et al. 1993). Another signature of magnetic activity is X-ray emission, originating in the hot corona (e.g., Pizzolato et al. 2003), as well as radio emission from electrons accelerated in the stellar magnetic field (e.g., Stewart et al. 1988; Berger 2006). Though, a random measurement of a chromospheric emission line or X-ray emission may capture an active flare and not be representative of a star's quiescent state (e.g., Paulson et al. 2006). An interesting feature of these magnetic activity signatures is the saturation with the stellar Rossby number, Ro, defined as the ratio of rotation period to the convective

turnover time. For Ro ≳ 0.1, stars show a log-linear relationship between the strength of magnetic indicators, normalized to stellar luminosity, and Rossby number, however, for Ro ≲ 0.1, the relationship is flat. As Ro probes magnetic field generation in the rotating and convecting stellar atmosphere, the saturation mechanism takes place somewhere in the rotating convection zone. The saturation is observed in Sun-like stars (e.g., Wilson 1966; Pallavicini et al. 1981) as well as M-dwarf stars on either side of the fully convective boundary (Newton et al. 2017; Wright et al. 2018).

The nature of the saturation mechanism in unclear. Proposed scenarios include centrifugal stripping of the corona (Jardine & Unruh 1999), however, this scenario does not explain saturation in the chromosphere and has since become a preferred explanation for super-saturation seen for Ro ≲ 0.01 in X-rays. Other proposed mechanisms include reaching a maximum filling factor of active regions in the photosphere or saturation of the dynamo mechanism itself (Vilhu 1984).

If the saturation mechanism were a process confined to the stellar chromosphere or corona, we would not expect *photospheric* magnetic activity indicators to saturate as well. However, Reiners et al. (2009) used Zeeman splitting in photospheric FeH lines of M dwarfs to show that the average unsigned magnetic field in the photosphere saturates as well. This suggests that the saturation mechanism lies at or beneath the stellar photosphere, and not in the chromosphere or corona. The investigation used rotational broadening of absorption lines instead of photometric rotation periods to estimate Rossby number and required an interpolation method to convert the FeH line profiles to an estimate of the unsigned magnetic field strength. Recently, Shulyak et al. (2019) measured unsigned average magnetic field strength using Ti I lines in the z band using data from the Calar Alto high-Resolution search for M dwarfs with Exoearths with

Near-infrared and optical Échelle Spectrographs (CARMENES; Quirrenbach et al. 2016). They used photometric rotation periods and compared the magnetic field strengths derived using FeH lines to the strength derived from z-band Ti I lines. They found that at high $v \sin i$ it is difficult to determine the magnetic field strength from FeH lines alone due to degeneracies in the derived parameters. However, they did not investigate the magnetic field strength as a function of Rossby number, and nearly all of the targets have Ro < 0.1, making it difficult to establish whether magnetic fields in the photosphere saturate across the Ro ∼ 0.1 saturation point.

In this paper, we report on the magnetic sensitivity of Ti I and Ca I absorption lines in the Y band, from 10000 to 11000 Å, versus Rossby number. The Y-band spectral region is entirely free of telluric absorption features, which typically plague infrared spectroscopy. We observed M-dwarf stars at high spectral-resolution in the Y band using the Near-Infrared Echelle Spectrograph (NIRSPEC) spectrograph on the Keck II Telescope, and we supplement our data with publicly available spectra from the CARMENES survey. The targets have a range of rotation periods, masses, and Rossby numbers. We find that the equivalent widths of these lines saturate in *absorption* for Ro < 0.1, similar to what is seen for X-rays and Hα in emission. The lines are magnetically enhanced (made *deeper*) due to the effect of Zeeman splitting on the curve of growth (see, for example, Basri et al. 1992). Our results provide further evidence that the fundamental magnetic saturation mechanism lies at or beneath the stellar photosphere.

2. Data

We collected spectra using one night of observation with the with the NIRSPEC on the 10 m Keck II Telescope located on the summit of Maunakea in Hawaii (McLean et al. 1998), and combine them with publicly available data from the CAR-MENES M-dwarf survey (Reiners et al. 2018). NIRSPEC is a cross-dispersed echelle spectrograph covering 1.0–5.0 μm in multiple settings, with a maximum resolving power ($\lambda/\Delta\lambda$) of 25,000. Wavelength regions within 1.0–5.0 μm are selected by the combination of a filter wheel and tilting/rotating motors mechanically connected to the echelle and cross-dispersing grating. In 2018, NIRSPEC was upgraded to improve slit-viewing, increase overall sensitivity, and increase the simultaneous wavelength coverage in a single setting (Martin et al. 2018). Most relevant to this work, the original 1024 × 1024 pixel InSb detector (20 μm pixels) was replaced with a larger and more sensitive 2048 × 2048 pixel HgCdTe detector (15 μm pixels). For this survey, we used the upgraded version of NIRSPEC on the night of UT 2019 December 18, the very first night of facility science operations of the upgraded instrument. The upgrade required some alternations to existing data reduction methods, which are described in Section 2.3.

2.1. NIRSPEC Target Selection

Targets for the NIRSPEC survey were chosen from Newton et al. (2017), who combined photometric rotation periods of M-dwarf targets in the MEarth transiting exoplanet survey (Charbonneau et al. 2009) with photometric rotation periods from the literature. We required targets to have a J magnitude of less than 11 and visibility from Maunakea. We then combined the measured rotational period with stellar radius, using the M_{Ks}-to-radius relationship from Mann et al. (2015) to

determine the maximum possible $v \sin i$. We combined trigonometric parallax measurements from ESA's *Gaia* Mission Gaia Collaboration (2018) with Ks-band photometry from the Two Micron All Sky Survey (2MASS; Skrutskie et al. 2006) to determine M_{Ks} for each target. We limited our targets to those with a maximum possible $v \sin i$ of 12 km s^{-1}, corresponding to the instrumental resolving power of NIRSPEC. We did this so that the rotational broadening would not significantly affect the resulting spectra. This resulted in 102 targets for the NIRSPEC sample. We then estimated their masses using the M_{Ks}-to-mass relationship from Mann et al. (2019).

The sample of M dwarfs from which we draw our targets for the NIRSPEC observations has been subject to substantial investigation by the MEarth team to identify known binaries. In that sample, data from the literature was used to identify eclipsing, visual, or spectroscopic binaries. Eclipsing binaries identified in the MEarth photometry (e.g., Dittmann et al. 2017; Winters et al. 2018) and in spectroscopic data identified through follow-up of MEarth targets (Newton et al. 2017) were noted. Stars overluminous for their color or spectroscopic properties based on relations from Newton et al. (2015) and Dittmann et al. (2016) were also noted as potential binaries. We selected only those stars not tagged as binaries or potential binaries. We note that the stellar binary fraction of M dwarfs (27%; Winters et al. 2019) is significantly lower than for higher mass stars.

2.2. NIRSPEC Observations

Of the 102 identified for NIRSPEC observations, we observed 30 on UT 2018 December 18. Conditions were photometric with an average seeing of 1″6. We used the NIRSPEC-1 mode and the 0″432 × 12″00 slit, which covers the Y band, roughly 9800 to 11000 Å, at a resolving power of $R = \lambda/\Delta\lambda = 25,000$. We acquired spectral dark images, flat-field images, and wavelength-calibrating arc-lamp images following the standard NIRSPEC observing procedure at the beginning of the night. We achieved a signal-to-noise ratio of between 60 and 100 across the Y band for each target.

In addition to the 30 M-dwarf targets, we also acquired spectra of a rapidly rotating A0 star, HD 43607, to provide a featureless spectrum for general calibration purposes. We observed all targets following an ABBA dither pattern on the slit, and read out the detector using multiple-correlated nondestructive double sampling (i.e., Fowler sampling; Fowler & Gatley 1990). Subtracting the AB (and BA) pairs removes detector fixed patterns and slowly varying background emission.

2.3. NIRSPEC Reduction

We reduced the data using a combination of the NIRSPEC Data Reduction Pipeline (NSDRP) software package (Tran et al. 2016), updated for the upgraded version of NIRSPEC, and custom routines. The NSDRP software package accepts spectral flat fields, arc-lamp images, and an AB pair of science observations, and returns a series of reduced data products. The software performs dark subtraction on the flat-field images, and divides the subtracted AB pair by the resulting flat-field image. Following the flat fielding, the software operates on each spectral order independently, rectifying the echellegram to remove curvature of the order and the slit tilt, producing a mean slit profile for each order and summing pixels across the regions of the slit profile that contain the target (one region for

the A image, one region for the B image) to produce spectra, then combines the A and B spectra into a single spectrum. The software then processes the arc-lamp images to provide a wavelength solution for each order. The program returns a two-dimensional rectified image, profile, spectrum, and uncertainty for each order.

To improve the signal-to-noise and bad-pixel rejection, we did not use the spectra returned by NSDRP and instead performed optimal extraction on the two-dimensional rectified images outputted by NSDRP for each order (see Horne 1986; Cushing et al. 2004, for a description of optimal extraction). As an optimal profile, we used the slit profile returned by NSDRP for each order. For each wavelength of each order, we fit the respective slit profile to the rectified image, allowing the normalization and additive offset of the profile to vary. The offset accounts for any remaining background that was not removed by the AB subtraction. After an initial fit, we removed data points that differed by more than 3σ from the fitted profile, then refit the profile. This approach rejected bad pixels (both "hot" pixels and "dead" pixels) from contaminating an entire wavelength bin.

Upon inspection of the resulting spectra, we found strong interference fringing effects with wavelength. The fringing is attributed to the combination of the order-sorting filter and the long-wavelength blocking filter in the NIRSPEC-1 mode, neither of which was replaced during the 2018 upgrade. To remove the fringing, we followed the same approach as Veyette et al. (2017). We Fourier transformed the spectrum of the featureless A0V star to find the frequencies of the fringes. We filtered the fringe frequencies in Fourier space with a finite impulse response notch filter based on a Hanning window with a width of 6×10^{-3} pix^{-1}. Following this procedure, we inspected the resulting A0V spectrum and found no evidence of fringing. We then applied an identical procedure to the 30 spectra.

2.4. CARMENES Spectra

CARMENES involves the combination of visible and near-infrared high-resolution spectrographs (Quirrenbach et al. 2016). The near-infrared spectrograph in CARMENES covers 9600 to 17100 Å with a resolving power of 80,400. Reiners et al. (2018) describe publicly available spectra of 324 M-dwarf stars from the CARMENES survey. We downloaded the CARMENES near-infrared spectra from the CARMENES data archive.[6] For each CARMENES order within the Y band, we convolved the data with a Gaussian kernel corresponding to an $R = 25,000$ spectrograph. Prior to convolution, the signal-to-noise of each publicly available spectrum was between 50 and 150 for each target. The CARMENES data contained several gaps in wavelength coverage. As we note below, we were unable to measure the equivalent width of one of the deep Ti I lines due to these gaps.

Díez Alonso et al. (2019) report rotational periods for 142 M dwarfs in the CARMENES survey, combining literature measurements with new photometric measurements. We chose to analyze targets with literature rotational periods, as we considered those to be the most reliable. Reiners et al. (2018) contain measurements of the $v \sin i$ of each spectrum, and as with the NIRSPEC data, we limited the sample to those with $v \sin i$ of less than 12 km s^{-1}. We determined the masses and radii of the stars in the same manner as with the NIRSPEC sample. Lastly, we visually inspected the resulting
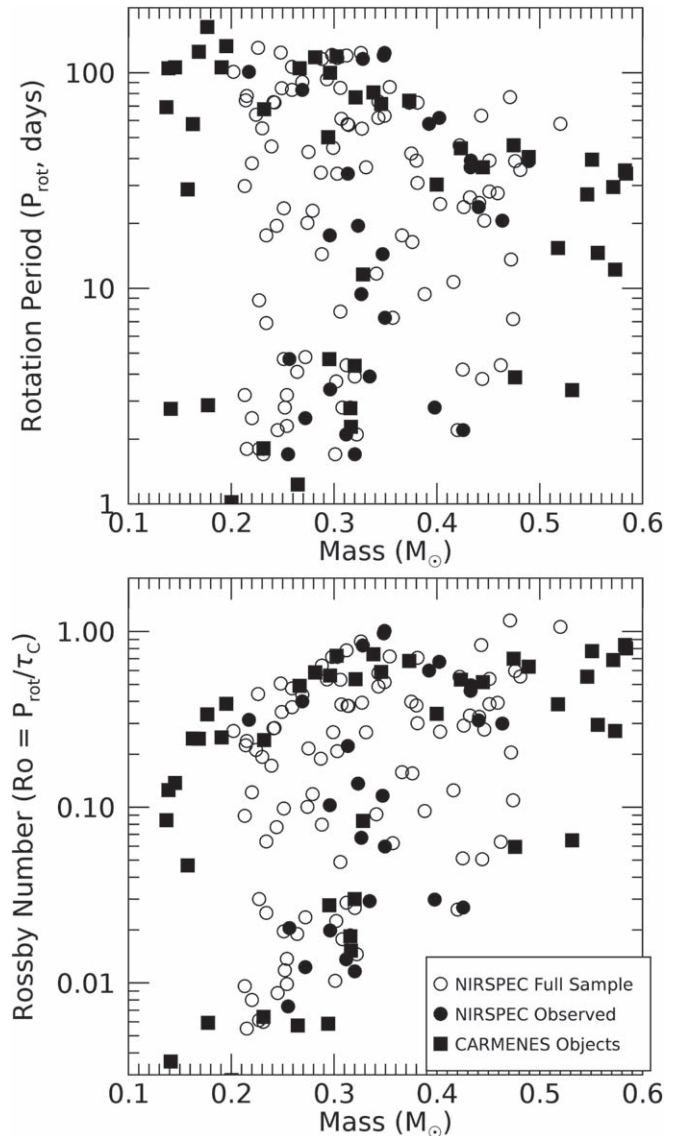
Figure 1. Mass vs. rotation period and Rossby number for the objects in the full sample and those observed. Masses were calculated using the mass–luminosity relations of Mann et al. (2019), rotation periods are from Newton et al. (2017), and convective turnover time was calculated using relations from Wright et al. (2011).

CARMENES spectra and removed one object owing to a significant amount of noise. Following these cuts, we were left with 44 M dwarfs in the CARMENES sample. Four of the 30 targets observed by NIRSPEC also have CARMENES data—HD 285968, G 99-49, V* YZ CMi, and G 195-36—resulting in 70 total objects with spectra in this work. We used these objects to assess our uncertainties in measured equivalent widths.

Table 1 lists the target properties and Figure 1 shows the full target sample and the observed targets versus rotational period and Rossby number for all 70 M dwarfs. Convective turnover time was calculated using relations from Wright et al. (2011). The M dwarfs cover a reasonable spread of masses, rotational periods, and Rossby numbers.

3. Analysis

For the combined 70 M dwarfs, we measured the equivalent widths of 10 Ti I lines originally identified by Veyette et al. (2017)

Table 1
Details on M-dwarf Stars in This Work

SIMBAD Name	α	δ	μ (mas)	π (mas)	K mag	Mass ($M_\odot$)	Sp. Type	P_{rot} (days)	log Ro	Inst.
BD+44 4548	$00^h05^m10^s89$	$+45°47'11\farcs64$	870.75, −151.27	86.96	5.85	0.52	M2Ve	15.37	−0.41	C
G 32-7	$00^h16^m16^s15$	$+19°51'50\farcs47$	708.09, −748.70	65.25	8.10	0.27	M4.0V	105.00	−0.31	C
G 32-37	$00^h39^m33^s55$	$+14°54'19\farcs07$	331.61, 34.76	34.82	9.12	0.31	M4.0V	34.00	−0.65	N
G 69-32	$00^h54^m48^s08$	$+27°31'03\farcs63$	341.47, 14.31	36.37	9.45	0.26	M4.5V	1.70	−2.13	N
Wolf 47	$01^h03^m19^s83$	$+62°21'55\farcs83$	730.74, 86.35	101.64	7.72	0.20	M5V	1.02	−2.55	C
YZ Cet	$01^h12^m30^s60$	$−16°59'56\farcs00$	−4410.43, 942.93	206.27	4.77	0.39	M1.0Ve	69.20	−0.15	C
2MASS J01192628+5450382	$01^h19^m26^s28$	$+54°50'38\farcs23$	166.39, −53.29	23.80	10.07	0.30	M4.5V	17.60	−0.99	N
G 159-46	$02^h12^m54^s62$	$+00°00'16\farcs86$	555.65, 29.00	65.45	8.17	0.26	M4V	4.70	−1.69	N
LP 197-37	$02^h40^m52^s42$	$+44°52'35\farcs07$	279.20, 90.21	45.25	8.46	0.33	M4V	9.40	−1.17	N
LP 356-15	$03^h24^m12^s86$	$+23°46'19\farcs06$	205.52, −110.35	48.45	7.45	0.46	M2.5Ve	20.60	−0.52	N
LP 413-24	$03^h39^m07^s13$	$+20°25'26\farcs71$	186.45, −39.49	28.00	9.71	0.30	M4.5	3.40	−1.70	N
G 80-21	$03^h47^m23^s34$	$−01°58'19\farcs95$	180.67, −274.18	59.52	6.93	0.48	M3.0V	3.87	−1.23	C
LP 357-119	$04^h02^m24^s42$	$+24°41'24\farcs42$	146.50, −147.32	33.13	8.47	0.43	M4.5	39.10	−0.31	N
GSC 05312-00079	$04^h14^m17^s31$	$−09°06'54\farcs61$	99.82, −145.46	40.30	8.76	0.32	M4.3V	1.70	−1.93	N
UCAC4 631-018323	$04^h30^m18^s23$	$+36°01'34\farcs26$	193.54, −20.76	33.69	8.43	0.43	M3.7V	36.40	−0.34	N
LP 834-32	$04^h35^m36^s19$	$−25°27'34\farcs59$	67.29, −195.92	59.61	7.41	0.40	M3.5	2.80	−1.53	N
HD 285968	$04^h42^m55^s78$	$+18°57'29\farcs39$	656.38, −1116.50	105.56	5.61	0.49	M2.5V	38.90	−0.20	B
RX J0451.0+3127	$04^h51^m01^s42$	$+31°27'23\farcs69$	232.32, −47.48	48.73	8.16	0.35	M3.7V	14.40	−0.93	N
G 100-46	$05^h53^m22^s97$	$+22°12'49\farcs78$	166.70, −195.10	34.25	9.09	0.32	M4V	19.50	−0.87	N
G 99-49	$06^h00^m03^s51$	$+02°42'23\farcs60$	309.49, −40.64	192.07	6.04	0.23	M3.5Ve	1.81	−2.19	B
G 192-15	$06^h02^m29^s19$	$+49°51'56\farcs16$	67.22, −850.07	104.89	8.44	0.14	M5.0V	105.00	−0.90	C
2MASS J06043887+0741545	$06^h04^m38^s87$	$+07°41'54\farcs55$	84.37, −193.67	22.95	9.78	0.35	M6V	7.30	−1.22	N
HD 42581	$06^h10^m34^s62$	$−21°51'52\farcs66$	−135.99, −719.09	173.70	4.17	0.55	M1V	27.30	−0.26	C
UCAC4 533-032549	$06^h44^m47^s52$	$+16°28'17\farcs84$	85.70, −139.76	26.03	9.24	0.39	M3V	57.90	−0.22	N
UCAC4 686-047574	$07^h10^m13^s42$	$+47°00'58\farcs01$	−78.69, −170.24	26.70	8.89	0.44	M3V	23.80	−0.51	N
LP 162-1	$07^h17^m08^s95$	$+45°45'54\farcs15$	81.17, −148.37	28.13	9.48	0.33	M4	115.80	−0.08	N
BD-02 2198	$07^h36^m07^s08$	$−03°06'38\farcs79$	68.24, −289.99	71.08	5.93	0.57	M1.0V	12.20	−0.57	C
UCAC4 480-038371	$07^h37^m43^s85$	$+05°54'36\farcs85$	−3.20, −153.64	27.26	9.08	0.40	M3V	61.70	−0.17	N
UCAC3 229-91098	$07^h38^m29^s50$	$+24°00'08\farcs65$	−152.14, −96.86	51.59	8.12	0.33	M2.7V	3.90	−1.53	N
V* YZ CMi	$07^h44^m40^s17$	$+03°33'08\farcs88$	−348.10, −445.88	167.02	5.70	0.32	M4.0Ve	2.80	−1.73	B
UCAC4 715-046733	$07^h55^m12^s08$	$+52°57'54\farcs01$	148.50, −52.97	41.48	9.06	0.27	M4	83.20	−0.40	N
G 50-21	$08^h10^m53^s62$	$+03°58'33\farcs61$	114.28, −340.07	45.64	8.29	0.35	M4V	123.40	0.00	N
UCAC4 468-040412	$08^h37^m30^s22$	$+03°33'45\farcs90$	61.72, −175.78	52.82	8.97	0.22	M4.0V	100.90	−0.50	N
UCAC4 608-044702	$08^h40^m15^s99$	$+31°27'06\farcs81$	205.54, 120.00	89.21	7.30	0.28	M3.5Ve	118.00	−0.23	C
G 46-27	$09^h11^m12^s70$	$+01°27'34\farcs87$	−20.36, −312.05	29.91	9.22	0.35	M4V	120.10	−0.01	N
G 195-36	$09^h42^m23^s19$	$+55°59'01\farcs26$	−710.24, −508.33	60.44	7.53	0.37	M3V	72.60	−0.17	B
BD+20 2465	$10^h19^m36^s28$	$+19°52'12\farcs02$	−498.61, −43.68	201.37	4.59	0.43	M4Vae	2.20	−1.57	N
G 196-37	$10^h36^m48^s15$	$+50°55'04\farcs03$	252.98, −206.70	41.85	9.02	0.27	M4.5V	2.50	−1.91	N
DS Leo	$11^h02^m38^s39$	$+21°58'01\farcs18$	−94.32, −671.25	58.91	6.55	0.54	M1	14.60	−0.55	C
LP 263-64	$11^h03^m09^s99$	$+36°39'08\farcs60$	−188.38, 30.09	43.81	8.63	0.31	M3.5V	2.10	−1.87	N
K2-18	$11^h30^m14^s52$	$+07°35'18\farcs26$	−80.38, −133.14	26.27	8.90	0.44	M3.5Ve	36.40	−0.29	C
Ross 1003	$11^h41^m44^s64$	$+42°45'07\farcs10$	−575.65, −89.97	90.76	6.82	0.35	M4.0Ve	71.50	−0.23	C
Ross 905	$11^h42^m11^s09$	$+26°42'23\farcs66$	895.05, −814.03	102.50	6.07	0.42	M3V	44.60	−0.27	C
G 10-49	$11^h47^m40^s75$	$+00°15'20\farcs10$	−314.20, −100.91	53.19	8.10	0.33	M4V	11.60	−1.08	C
FI Vir	$11^h47^m44^s36$	$+00°48'17\farcs14$	−326.00, −323.00	67.07	7.56	0.33	M3V	163.00	0.09	C
G 122-49	$11^h50^m57^s72$	$+48°22'38\farcs56$	−1545.70, −962.82	124.41	7.64	0.17	M7	125.00	−0.61	C
Ross 689	$12^h05^m29^s68$	$+69°32'22\farcs60$	−456.97, −55.21	64.70	7.89	0.30	M4V	100.00	−0.25	C
G 177-25	$13^h10^m12^s63$	$+47°45'18\farcs68$	−636.17, −616.24	82.03	8.69	0.16	M5.0V	28.80	−1.33	C

4

Table 1
(Continued)

SIMBAD Name	α	δ	μ (mas)	π (mas)	K mag	Mass ($M_\odot$)	Sp. Type	$P_{\rm rot}$ (days)	log Ro	Inst.
NLTT 35712	$13^{\rm h}53^{\rm m}38\overset{\rm s}{.}80$	$+77°37'08\overset{''}{.}14$	224.14, −15.14	75.47	7.80	0.26	M4.0V	1.23	−2.24	C
OT Ser	$15^{\rm h}21^{\rm m}52\overset{\rm s}{.}88$	$+20°58'38\overset{''}{.}79$	2891.52, 411.90	280.69	4.02	0.40	M2V	3.37	−1.44	C
G 202-48	$16^{\rm h}25^{\rm m}24\overset{\rm s}{.}62$	$+54°18'14\overset{''}{.}76$	432.07, −171.67	154.47	5.83	0.32	M1.5V	76.79	−0.27	C
BD-12 4523	$16^{\rm h}30^{\rm m}18\overset{\rm s}{.}06$	$-12°39'45\overset{''}{.}32$	−94.03, −1183.78	232.21	5.07	0.30	M3V	119.00	−0.14	C
G 204-39	$17^{\rm h}57^{\rm m}50\overset{\rm s}{.}97$	$+46°35'19\overset{''}{.}13$	−15.18, 578.30	71.48	7.00	0.40	M2.5V	30.30	−0.47	C
LP 390-16	$18^{\rm h}13^{\rm m}06\overset{\rm s}{.}57$	$+26°01'51\overset{''}{.}86$	221.10, −37.19	56.01	8.06	0.32	M4.0V	2.28	−1.82	C
BD+45 2743	$18^{\rm h}35^{\rm m}18\overset{\rm s}{.}39$	$+45°44'38\overset{''}{.}54$	452.19, 363.67	64.25	6.08	0.58	M0.5V	34.00	−0.10	C
Ross 149	$18^{\rm h}36^{\rm m}19\overset{\rm s}{.}23$	$+13°36'26\overset{''}{.}37$	179.14, 278.91	83.03	7.37	0.29	M4V	50.20	−2.23	C
G 141-36	$18^{\rm h}48^{\rm m}17\overset{\rm s}{.}53$	$+07°41'21\overset{''}{.}18$	376.33, 249.30	131.20	7.91	0.14	M5.0V	2.76	−2.45	C
Ross 154	$18^{\rm h}49^{\rm m}49\overset{\rm s}{.}37$	$-23°50'10\overset{''}{.}45$	639.35, −193.55	336.12	5.37	0.18	M3.5Ve	2.87	−2.23	C
HD 176029	$18^{\rm h}58^{\rm m}00\overset{\rm s}{.}14$	$+05°54'29\overset{''}{.}24$	−196.30, −1220.47	90.05	5.36	0.58	M1.0Ve	35.20	−0.08	C
HD 180617	$19^{\rm h}16^{\rm m}55\overset{\rm s}{.}25$	$+05°10'08\overset{''}{.}04$	−579.04, −1332.74	169.16	4.67	0.47	M3-V	46.00	−0.15	C
G 185-18	$19^{\rm h}21^{\rm m}38\overset{\rm s}{.}70$	$+20°52'03\overset{''}{.}27$	−948.34, −1455.73	94.20	7.93	0.20	M4.0Ve	133.00	−0.41	C
Wolf 1069	$20^{\rm h}26^{\rm m}05\overset{\rm s}{.}30$	$+58°34'22\overset{''}{.}68$	261.08, 542.99	104.32	8.10	0.16	M4.95	57.70	−0.61	C
G 144-25	$20^{\rm h}40^{\rm m}33\overset{\rm s}{.}86$	$+15°29'58\overset{''}{.}73$	1321.00, 662.23	104.89	7.75	0.19	M4.5V	106.00	−0.60	C
LP 816-60	$20^{\rm h}52^{\rm m}33\overset{\rm s}{.}01$	$-16°58'29\overset{''}{.}01$	−309.22, 37.35	178.12	6.20	0.23	M4V	67.60	−0.62	C
HD 209290	$22^{\rm h}02^{\rm m}10\overset{\rm s}{.}28$	$+01°24'00\overset{''}{.}83$	−452.43, −278.58	94.74	5.32	0.57	M0.5V	29.50	−0.16	C
EV Lac	$22^{\rm h}46^{\rm m}50\overset{\rm s}{.}70$	$+44°20'08\overset{''}{.}00$	−483.17, 89.27	92.90	6.07	0.46	M3.0Ve	4.38	−1.20	C
IL Aqr	$22^{\rm h}53^{\rm m}16\overset{\rm s}{.}50$	$-14°15'48\overset{''}{.}00$	−94.32, −671.25	58.91	6.55	0.54	M1	81.00	0.29	C
HD 216899	$22^{\rm h}56^{\rm m}34\overset{\rm s}{.}80$	$+16°33'12\overset{''}{.}36$	−1034.80, −284.00	145.61	4.52	0.55	M1.5Ve	39.50	−0.11	C
HH And	$23^{\rm h}41^{\rm m}54\overset{\rm s}{.}00$	$+44°10'46\overset{''}{.}00$	748.11, 480.60	190.26	5.95	0.24	M4.0Ve	106.00	−0.41	C
RX J2354.8+3831	$23^{\rm h}54^{\rm m}51\overset{\rm s}{.}46$	$+38°31'36\overset{''}{.}20$	−131.57, −86.11	59.35	8.09	0.30	M3.1V	4.70	−1.56	C

Note. All astrometric data are from *Gaia* DR2 in the International Celestial Reference System (ICRS) and epoch 2000 (Gaia Collaboration 2018). *K*-band magnitudes are from the Two Micron All Sky Survey Point Source Catalog (2MASS; Cutri et al. 2003; Skrutskie et al. 2006). Masses were calculated using the M_K-to-mass relations of Mann et al. (2019). Spectral types are from SIMBAD. Rotation periods are from Newton et al. (2017) for targets with NIRSPEC observations and from Díez Alonso et al. (2019) for CARMENES data. For targets with both, we default to the Newton et al. (2017) rotation periods. Convective turnover time was calculated using the mass-dependent relation from Wright et al. (2011). "C" refers to CARMENES, "N" refers to NIRSPEC, and "B" indicates both NIRSPEC and CARMENES.

(This table is available in its entirety in machine-readable form.)

Table 2
Ti I Absorption Line Properties

Line	Wavelength in Air (Å)	Lower Energy (wn)	Lower State	Upper State	log gf	Landé g_{eff}
Ca I	10343.8194	23652.3040	3p6.4s.4p 1P*	3p6.4s.5s 1S	−0.300	1.00
Ti I (1)	10396.802	6842.965	3d3.(2G).4s a3G	3d2.(3F).4s.4p.(1P*) y3F*	−1.54	1.13
Ti I (2)	10496.113	6742.755	3d3.(4F).4s b3F	3d2.(3F).4s.4p.(3P) z3G*	−1.65	1.05
Ti I (3)	10584.633	6661.004	3d3.(2D2).4s a3D	3d2.(1D).4s.4p.(3P*) x3D*	−1.77	1.00
Ti I (4)	10677.047	6742.755	3d3.(4F).4s a5F	3d2.(3F).4s.4p.(3P*) z5G*	−2.52	1.25
Ti I (5)	10726.391	6556.833	3d3.(4F).4s a5F	3d2.(3F).4s.4p.(3P*) z5G*	−2.06	0.59
Ti I (6)	10774.866	6598.764	3d3.(4F).4s a5F	3d2.(3F).4s.4p.(3P*) z5G*	−2.67	0.69

Note. Line properties were accessed from the VALD3 database (Piskunov et al. 1995; Ryabchikova et al. 2015). Line data originates from Kurucz (2010).

as tracers of Ti abundance in M-dwarf stars. We used the `analyze_NIRSPEC1` software pipeline to measure equivalent widths, available on GitHub. See Veyette et al. (2017) for a detailed description of the method for measuring equivalent widths, which we briefly summarize here. Spectra of M-dwarf stars contain significant molecular features across all wavelengths, which result in a pseudocontinuum useful for measuring equivalent widths. In the Y band, the dominant source of molecular opacity is FeH.

First, we cross-correlated each spectrum with synthetic spectra from the BT-Settl atmosphere database (Allard et al. 2012) in order to remove any radial velocity shifts. To estimate the pseudocontinuum, first we removed high-frequency variations in the spectrum with a second-order Savitzky–Golay filter with a window length of five pixels (Savitzky & Golay 1964). We then applied a running maximum filter with a width of seven resolution elements to establish a ceiling to the features. Lastly, we fitted a sixth-order Chebyshev polynomial to the filtered spectrum, which was taken as the pseudocontinuum for measuring equivalent widths.

Of the 10 Ti I lines identified by Veyette et al. (2017), we report on the six deepest lines for the NIRSPEC data and five lines for the CARMENES data. Both the NIRSPEC and CARMENES data also include a deep Ca I line, which we also report. Table 2 displays the properties of these six lines, which we refer to as Ti I (1) to Ti I (6). The CARMENES data is missing the Ti I (5) line due to gaps in the publicly available spectra near the edge of the line.

The line properties were retrieved from the Third Vienna Atomic Line Database (VALD3; Piskunov et al. 1995; Ryabchikova et al. 2015) and the line data originates from Kurucz (2010). All of the Ti I lines have similar lower energy states, but with a range of absorption cross-sections, parameterized as the log of the transition oscillator strength (f) times the statistical weight (g), and effective Landé g factors.

For the four stars with both NIRSPEC and CARMENES data, we used the differences in the equivalent width determinations as a rubric for uncertainties. Figure 2 plots the equivalent widths measured from the NIRSPEC data versus those measured from the CARMENES data for the same stars. The CARMENES equivalent widths are systematically lower than the NIRSPEC equivalent widths by 0.011 Å, and the standard deviation of the differences is 0.018 Å. Since the systematic difference is within the standard deviation, we do not apply any corrections to the CARMENES equivalent widths. We adopt 0.018 Å as the uncertainty in all equivalent width measurements. We adopt this value as a conservative estimate of the typical uncertainties, as it incorporates systematic errors in the equivalent width calculation that are
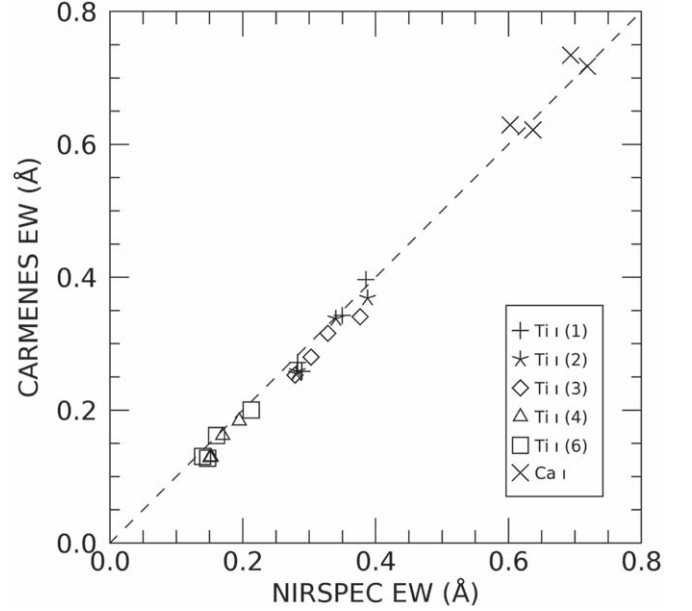

Figure 2. Equivalent widths of the Ti I and Ca I lines in the Y band measured using NIRSPEC data vs. CARMENES data on the same stars. The dashed line represents a one-to-one correspondence. The CARMENES equivalent widths are systematically lower than the NIRSPEC equivalent widths by 0.011 Å, and the standard deviation of the differences is 0.018 Å.

difficult to include via canonical error propagation. All of the spectra have similar signal-to-noise values and we do not expect much variation in the equivalent width uncertainties between objects.

Figure 3 and the accompanying online figure set show the resulting continuum-normalized and zero-velocity spectra as well as the lines used in this work. Table 3 lists the resulting equivalent widths for the six Ti I lines and one Ca I line.

Figure 4 clearly shows an increase in Ti I equivalent widths with decreasing Rossby number despite the appearance of several outlying measurements. Visual inspection suggests that the equivalent widths saturate for Ro $\lesssim$ 0.1, as is seen in Hα, X-ray emission, and FeH broadening, for most of the lines analyzed. We attribute the trend and saturation to magnetic enhancement of the lines. For deep absorption lines with saturated line cores (saturation here referring to the physical saturation of the line core, not the saturation of equivalent width with Rossby number), Zeeman splitting can dramatically increase the line equivalent width, even if the total number of absorbing atoms remains the same. This effect occurs prior to stellar rotational broadening and instrumental broadening, so
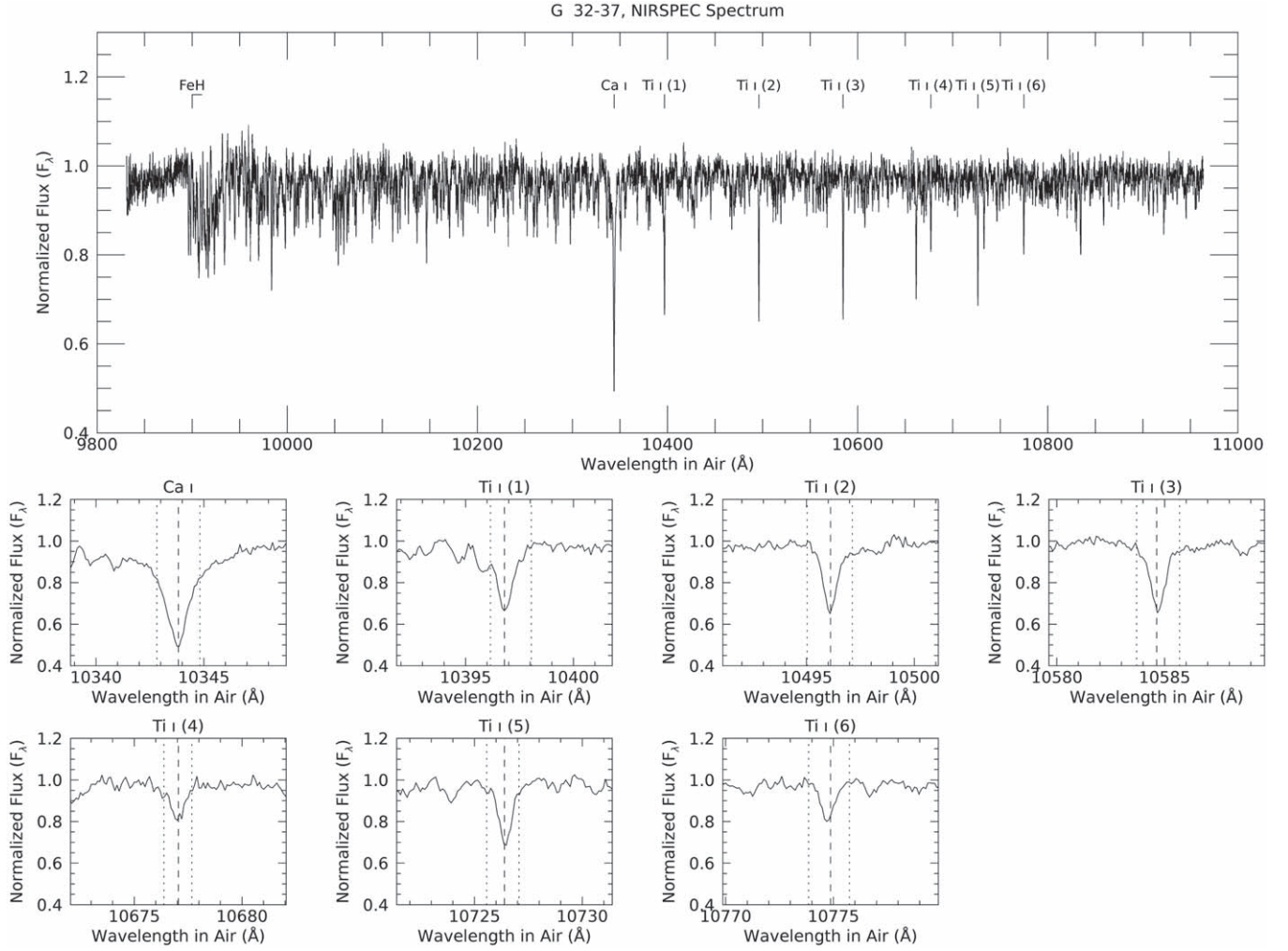
Figure 3. Top: full *Y*-band spectrum continuum-normalized and shifted to zero velocity with features indicated. Bottom: close-up on the Ti I lines used in this analysis, with the VALD transition wavelength (dashed line) and limits of the equivalent width calculation (dotted lines) indicated.

(The complete figure set (74 images) is available.)

the effect of increased equivalent width can occur in lines that do not appear saturated in measured spectra, even if they have saturated line cores, as is the case here.

Figure 5 is identical to Figure 4, except with mass on the *x*-axis and points colored by Rossby number. We see some equivalent width dependence on stellar mass (and correspondingly effective temperature), however, at a fixed mass, the increase and saturation with equivalent width with Rossby number is evident, especially around 0.3 $M_{\odot}$.

We note that several objects appear as outliers in Figure 4. For Ti I (6), the CARMENES spectra of G 144-25, HD 216899, and Ross 248 appear to be contaminated by bad pixels, leading to erroneously large equivalent width determinations. Similarly, for Ti I (4), the CARMENES spectra of Wolf 1069 and Ross 248 appear to be contaminated by bad pixels, resulting in erroneous equivalent width determinations.

3.1. The Curve of Growth

Since the Ti I lines originate from the same atomic species and ionization state, and the energies of the lower and upper states are similar, they can be plotted on a curve-of-growth diagram, showing equivalent width versus log (*gf*). Figure 6

shows the resulting curve-of-growth diagrams for the lines, colored by stellar mass and by Rossby number (Ro). Whereas the curves of growth do not show a clear dependence on stellar mass, they do show a dependence on Rossby number.

The relatively small increase in equivalent width versus *gf* (a factor of two in equivalent width versus a decade in *gf*) suggests that all six lines are located in either the saturated regime or the damping regime of the curve of growth, not the linear regime. Lines in the saturated or damping regime are especially susceptible to magnetic enhancement via Zeeman splitting: as saturated lines split, the equivalent width increases. The location on the curve of growth is further evidence that the increase in equivalent width with Rossby number is due to magnetic enhancement and not a nonmagnetic source, which we explore further in the next section.

It is curious that the spread in equivalent width values for a given line in Figure 6 does not appear to depend on the effective Landé *g* factor ($g_{\rm eff}$) of the corresponding transition. The lines with the lowest $g_{\rm eff}$, Ti I (5), and Ti I (6), both under 1, show just as much of a spread in equivalent width as the transitions with Landé *g* factors greater than 1. We cannot explain this apparent lack of dependence on $g_{\rm eff}$. We note that the $g_{\rm eff}$ factors for these particular Ti I lines are well known. Ti I lines with similar lower

Table 3
Ti I Equivalent Widths (Å)

SIMBAD Name	Ti I (1)	Ti I (2)	Ti I (3)	Ti I (4)	Ti I (5)	Ti I (6)	Ca I	NIRSPEC/CARMENES
BD+44 4548	0.2464	0.2415	0.2905	0.1206		0.1187	0.6002	CARMENES
G 32-7	0.2526	0.2570	0.2502	0.1329		0.1228	0.6265	CARMENES
G 32-37	0.3272	0.3099	0.3179	0.1587	0.2425	0.1634	0.6735	NIRSPEC
G 69-32	0.3501	0.3221	0.3349	0.1739	0.2703	0.1799	0.6954	NIRSPEC
Wolf 47	0.3519	0.3865	0.3553	0.1777		0.1963	0.7147	CARMENES
V* YZ Cet	0.3677	0.3649	0.3432	0.1721		0.1560	0.7348	CARMENES
2MASS J01192628+5450382	0.4110	0.3785	0.3544	0.2135	0.3083	0.2249	0.7190	NIRSPEC
G 159-46	0.3277	0.3313	0.3146	0.1604	0.2511	0.1636	0.6793	NIRSPEC
LP 197-37	0.3076	0.3068	0.2928	0.1226	0.2085	0.1291	0.6435	NIRSPEC
LP 356-15	0.2978	0.2828	0.3106	0.1476	0.2221	0.1456	0.6408	NIRSPEC
LP 413-24	0.3401	0.3297	0.3136	0.1698	0.2662	0.1788	0.6928	NIRSPEC
G 80-21	0.3408	0.3237	0.3287	0.1716		0.1740	0.6781	CARMENES
LP 357-119	0.3212	0.3062	0.3275	0.1673	0.2391	0.1718	0.6499	NIRSPEC
GSC 05312-00079	0.3805	0.3656	0.3646	0.1815	0.2917	0.1802	0.7248	NIRSPEC
UCAC4 631-018323	0.2881	0.2795	0.2852	0.1210	0.2130	0.1186	0.5919	NIRSPEC
LP 834-32	0.3701	0.3388	0.3475	0.1908	0.2521	0.1942	0.7175	NIRSPEC
HD 285968	0.2889	0.2808	0.3028	0.1506	0.2187	0.1472	0.6024	NIRSPEC
HD 285968	0.2584	0.2547	0.2798	0.1288		0.1277	0.6294	CARMENES
RX J0451.0+3127	0.3523	0.3273	0.3335	0.1628	0.2766	0.1786	0.6868	NIRSPEC
G 100-46	0.3200	0.3557	0.3216	0.1593	0.2130	0.1994	0.5862	NIRSPEC
G 99-49	0.3424	0.3378	0.3157	0.1620		0.1617	0.7342	CARMENES
G 99-49	0.3497	0.3402	0.3281	0.1698	0.2703	0.1605	0.6937	NIRSPEC
G 192-15	0.3063	0.3357	0.3114	0.1688		0.1681	0.6836	CARMENES
2MASS J06043887+0741545	0.3306	0.2809	0.2989	0.1464	0.2312	0.1941	0.6583	NIRSPEC
HD 42581	0.2524	0.2422	0.3067	0.1301		0.1137	0.5997	CARMENES
UCAC4 533-032549	0.2820	0.2656	0.2705	0.1369	0.2069	0.1289	0.6219	NIRSPEC
UCAC4 686-047574	0.3022	0.2859	0.3140	0.1582	0.2289	0.1459	0.6497	NIRSPEC
LP 162-1	0.2931	0.2689	0.2745	0.1443	0.2255	0.1271	0.5964	NIRSPEC
BD-02 2198	0.2627	0.2574	0.3299	0.1433		0.1315	0.5995	CARMENES
UCAC4 480-038371	0.2776	0.2698	0.2836	0.1413	0.2107	0.1257	0.6218	NIRSPEC
UCAC3 229-91098	0.3619	0.3541	0.3561	0.1727	0.2733	0.1708	0.7049	NIRSPEC
V* YZ CMi	0.3854	0.3878	0.3767	0.1947	0.3101	0.2126	0.7187	NIRSPEC
V* YZ CMi	0.3965	0.3686	0.3405	0.1839		0.2002	0.7174	CARMENES
UCAC4 715-046733	0.2881	0.2758	0.2708	0.1315	0.2149	0.1345	0.6319	NIRSPEC
G 50-21	0.2809	0.2626	0.2642	0.1385	0.2206	0.1263	0.6072	NIRSPEC
UCAC4 468-040412	0.2963	0.2879	0.2730	0.1518	0.2284	0.1363	0.6368	NIRSPEC
UCAC4 608-044702	0.2706	0.2551	0.2521	0.1236		0.1125	0.6298	CARMENES
G 46-27	0.2879	0.2738	0.2670	0.1434	0.2132	0.1528	0.6321	NIRSPEC
G 195-36	0.2825	0.2820	0.2786	0.1523	0.2125	0.1396	0.6368	NIRSPEC
G 195-36	0.2717	0.2584	0.2528	0.1298		0.1305	0.6216	CARMENES
BD+20 2465	0.3551	0.3312	0.3440	0.1844	0.2655	0.1997	0.6515	NIRSPEC
G 196-37	0.3575	0.3919	0.3206	0.1590	0.2722	0.1846	0.6906	NIRSPEC
V* DS Leo	0.2604	0.2528	0.3228	0.1306		0.1303	0.6086	CARMENES
LP 263-64	0.3758	0.3748	0.3656	0.1673	0.2760	0.1949	0.7187	NIRSPEC
K2-18	0.2937	0.2566	0.2488	0.1275		0.1455	0.6243	CARMENES
Ross 1003	0.2701	0.2536	0.2499	0.1332		0.1326	0.6387	CARMENES
Ross 905	0.2620	0.2514	0.2646	0.1240		0.1146	0.6226	CARMENES
G 10-49	0.3679	0.3612	0.3336	0.1807		0.1891	0.7340	CARMENES
Ross 128	0.2567	0.2477	0.2666	0.1128		0.1088	0.6045	CARMENES
G 122-49	0.2786	0.3097	0.2918	0.1541		0.1509	0.6768	CARMENES
Ross 689	0.2771	0.2568	0.2526	0.1290		0.1239	0.6390	CARMENES
G 177-25	0.3292	0.3633	0.3470	0.1772		0.1894	0.7136	CARMENES
NLTT 35712	0.2986	0.3359	0.3221	0.1642		0.1793	0.7141	CARMENES
V* OT Ser	0.3349	0.3241	0.3541	0.1711		0.1880	0.6921	CARMENES
G 202-48	0.2597	0.2494	0.2594	0.1168		0.1001	0.6026	CARMENES
BD-12 4523	0.2228	0.2133	0.2114	0.0999		0.1393	0.5419	CARMENES
G 204-39	0.2590	0.2562	0.2696	0.1313		0.1537	0.6534	CARMENES
LP 390-16	0.3330	0.3692	0.3415	0.1841		0.2028	0.7206	CARMENES
BD+45 2743	0.2381	0.2248	0.3225	0.1049		0.1420	0.5610	CARMENES
Ross 149	0.2994	0.3226	0.3065	0.1546		0.2394	0.7162	CARMENES
G 141-36	0.2996	0.3579	0.3357	0.1847		0.2080	0.7949	CARMENES
Ross 154	0.3404	0.3334	0.3200	0.1651		0.1443	0.7007	CARMENES
HD 176029	0.2413	0.2401	0.3247	0.1221		0.1197	0.5879	CARMENES
HD 180617	0.2605	0.2494	0.2758	0.1290		0.1152	0.6160	CARMENES

Table 3
(Continued)

SIMBAD Name	Ti I (1)	Ti I (2)	Ti I (3)	Ti I (4)	Ti I (5)	Ti I (6)	Ca I	NIRSPEC/CARMENES
G 185-18	0.2947	0.2699	0.2550	0.1402		0.1296	0.6373	CARMENES
Wolf 1069	0.3399	0.2701	0.2771	0.2293		0.2046	0.5909	CARMENES
G 144-25	0.3064	0.2802	0.2771	0.1522		0.3304	0.6658	CARMENES
LP 816-60	0.2698	0.2707	0.2649	0.1421		0.1252	0.6472	CARMENES
HD 209290	0.2446	0.2300	0.3237	0.1238		0.1156	0.5904	CARMENES
V* EV Lac	0.3607	0.3535	0.3408	0.1666		0.1681	0.7183	CARMENES
BD-15 6290	0.2659	0.2570	0.2555	0.1422		0.1220	0.6355	CARMENES
HD 216899	0.2630	0.2441	0.3134	0.1294		0.3008	0.6179	CARMENES
Ross 248	0.3437	0.2958	0.2850	0.2668		0.3048	0.6356	CARMENES
RX J2354.8+3831	0.3655	0.3636	0.3347	0.1606		0.1708	0.7077	CARMENES

(This table is available in its entirety in machine-readable form.)
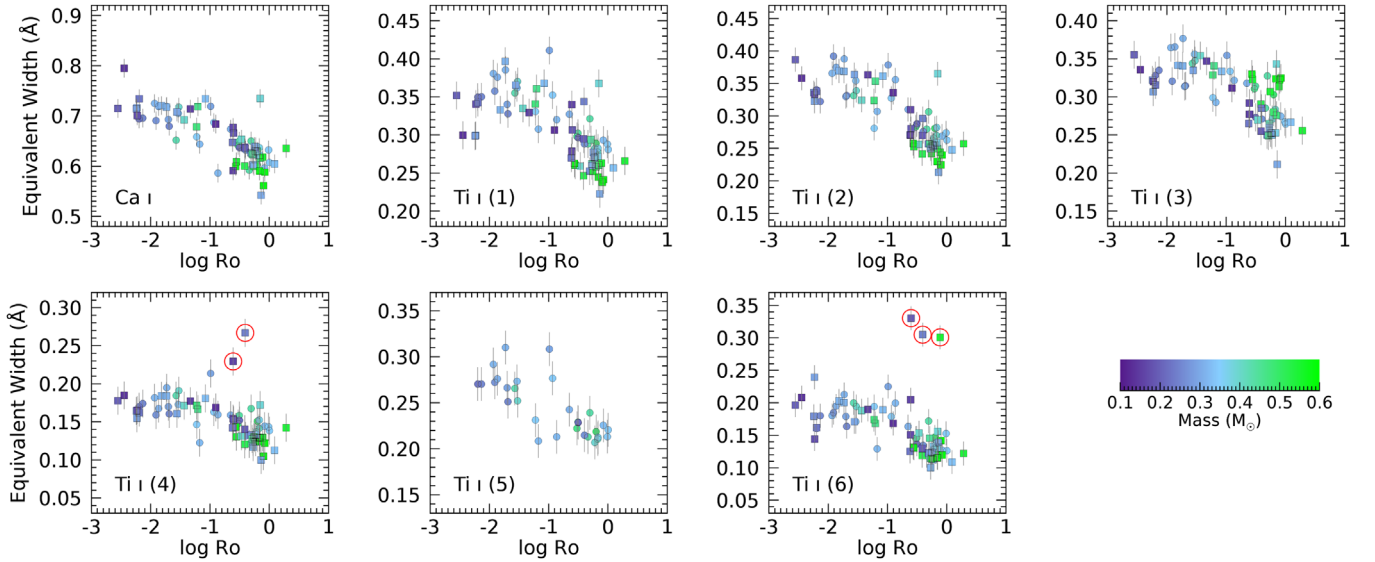
Figure 4. Equivalent width vs. Rossby number (Ro) for the Ca I and Ti I lines of the 70 M dwarfs in the combined NIRSPEC and CARMENES samples. M dwarfs with NIRSPEC data are shown as circles; M dwarfs with CARMENES data are shown as squares. We lack CARMENES data for the Ti I (5) line. The color bar indicates the M-dwarf mass, determined using mass–luminosity relationships from Mann et al. (2019). The outliers in Ti I (4) and Ti I (6) appear to be due to contaminated CARMENES spectra and are marked with a red circle.
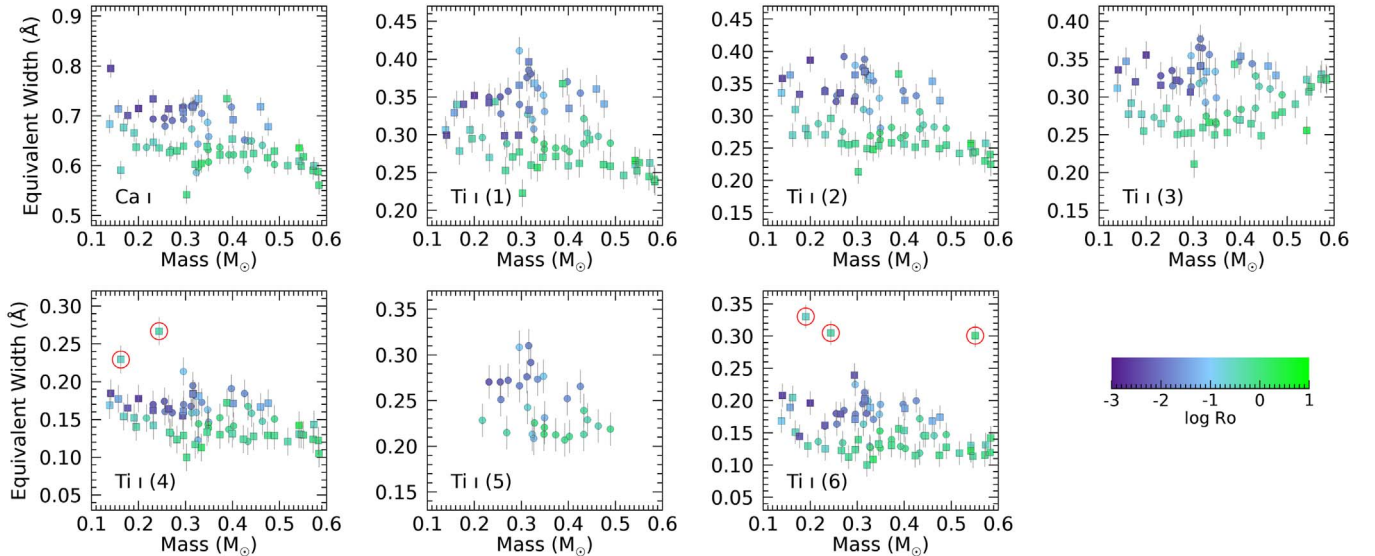
Figure 5. Same as Figure 4, but with stellar mass on the x-axis and colored by Rossby number. There is some mass/temperature dependence to the equivalent widths, however, at a fixed mass, we see an increase in equivalent width with Rossby number.
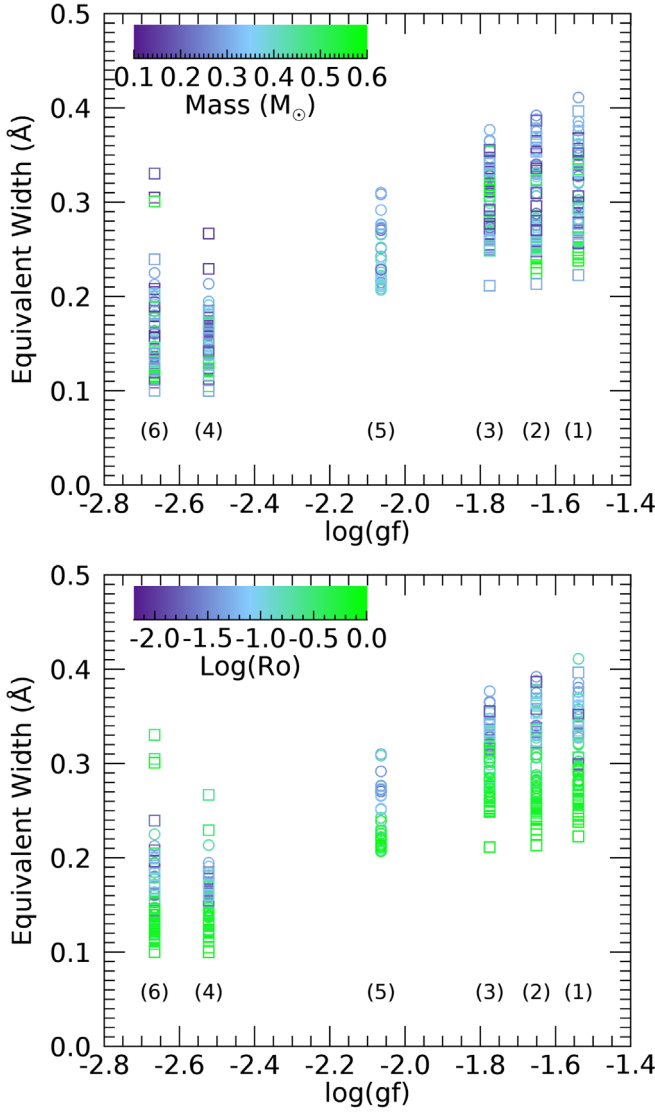
Figure 6. Equivalent width vs. the log of the oscillator strength f times the number of degenerate states g (the curve of growth) for the six Ti I lines in this study, colored by stellar mass (top) and by log of the Rossby number (bottom). Measurements from the NIRSPEC data are circles and measurements from the CARMENES data are squares. The sublinear increase in equivalent width with gf suggests that the lines are in the saturated or damping regime and are therefore subject to magnetic enhancement.

and upper energy levels have been used in previous investigations of magnetic fields on M dwarfs (Shulyak et al. 2017, 2019) and on sunspots (Shulyak et al. 2010). We leave a detailed investigation into the magnetic field strength associated with the observed Zeeman enhancement to a future paper.

We note that the equivalent widths show no obvious correlation with stellar mass, and correspondingly, stellar effective temperature. Being in the saturated regime of the curve of growth, the equivalent widths should be relatively insensitive to temperature, as the column density of Ti I atoms in these particular electron configurations should have a weak impact on the measured equivalent width. Indeed, in Figure 5, we see a weak dependence on stellar mass.

3.2. Nonmagnetic Sources for the Trend

We rule out the following sources for the trend in equivalent width versus Rossby number: rotational broadening, Ti

abundance, and mass/temperature/gravity. Regarding rotational broadening, objects were specifically chosen such that rotational broadening would not significantly affect the resulting line profiles. We also argue that Ti abundance cannot be responsible either, although differences in Ti abundance may well be responsible for the scatter. Ti abundance does not explain the saturation seen for Ro $\lesssim$ 0.1, consistent with Hα and X-ray emission.

Temperature, mass, and surface gravity are other potential explanations for the trends and saturation, however, we include a wide range of stellar masses (and corresponding temperatures and surface gravities) in this sample. In Figure 5, we see similar behavior in equivalent width versus Rossby number as a function of mass. We therefore rule this out as an explanation.

3.3. Saturation Value

We aim to compare the saturation behavior of Ti I equivalent widths to chromospheric and coronal emission. For each of the six lines, we fit a function to the equivalent width versus Rossby number using same function form used for Hα and X-ray emission (Wright et al. 2011, 2018; Newton et al. 2017):

$$EW = \begin{array}{ll} EW_{sat}, & Ro \leqslant Ro_{sat} \\ CR_o^{\beta}, & R_o > R_{sat}, \end{array} \qquad (1)$$

where C is fixed to a constant to ensure continuity between regimes. We note that in Figure 4, the equivalent widths are on a linear scale, whereas chromospheric and coronal emission are often varying on a logarithmic scale, resulting in very different values for β. For each line, we fit this functional form to the data using a Levenburg–Marquardt optimization routine (Levenberg 1944; Marquardt 1963). We removed the outliers discussed above from the fitted data.

In order to correct for the small variations in equivalent width with stellar mass, as seen in Figure 5, we limited our targets to those with masses between 0.25 and 0.35 $M_{\odot}$ in the fitting routine. Figure 7 shows the resulting fits and Table 4 lists the resulting values. We include a calculation of the difference in Bayesian Inference Criterion (BIC; Schwarz 1978) between the fitted saturation model and a fitted log-linear model (i.e., a line versus log Ro). The BIC parameter favors models with a better fit to the data while penalizing models for excessive model parameters. Values lower than −10 indicate a strong preference for the saturation model, values between than −10 and 0 indicate weak to no preference, and values between 0 and 10 indicate weak to no preference for the log-linear model. The saturation model is strongly preferred for Ti I (1), (2), and (3). For Ca I and Ti I (4) and (6) the saturation model is weakly preferred, and for Ti I (5) a log-linear model is somewhat preferred.

We find a remarkably similar saturation value of Ro for all of the Ti I lines near Ro = 0.1. The saturation values are similar to what is seen in the chromospheric saturation of M dwarf stars. Newton et al. (2017) found a value of Ro$_{sat}$ = 0.21 ± 0.02 for the saturation of Hα with Rossby number, and Wright et al. (2018) found a value of $Ro_{sat} = 0.14^{+0.08}_{-0.04}$ for the X-ray emission for fully convective M dwarfs. Douglas et al. (2014) found a value of $0.11^{+0.02}) − 0.03$ for K and M dwarfs in the Hyades cluster. The similarity in saturation value for the Ti I equivalent widths and Hα and X-ray emission provides strong evidence that the Ti I lines are magnetically enhanced.
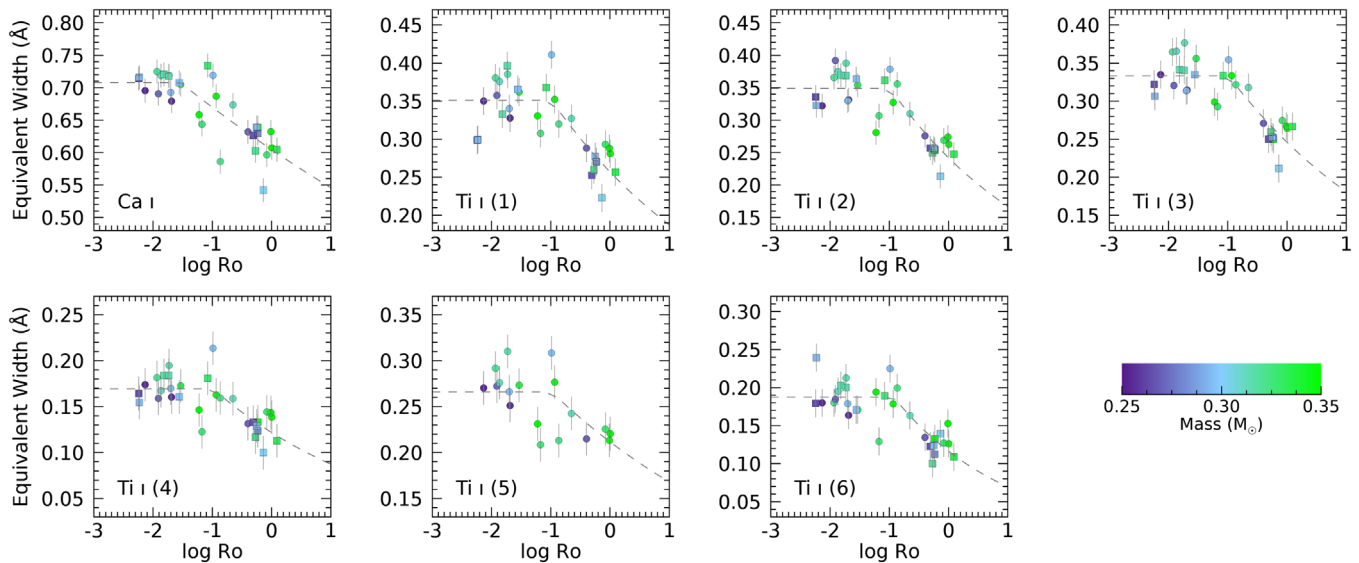
Figure 7. Same as Figure 4, but including model fits to the saturation with Rossby number (dashed lines). We also limit the targets to those with masses between 0.25 and 0.35 $M_\odot$, where we have a wide range of Rossby numbers in our sample, to reduce the effect of stellar mass and temperature.

Table 4
Fitted Parameters

Line	C	β	R_{sat}	ΔBIC
Ca I	0.7079	−0.0445	0.0288	−1.6
Ti I (1)	0.3510	−0.1370	0.1024	−35.5
Ti I (2)	0.3489	−0.1608	0.1027	−21.8
Ti I (3)	0.3332	−0.1336	0.1027	−13.8
Ti I (4)	0.1693	−0.1446	0.1027	−2.7
Ti I (5)	0.2660	−0.1003	0.1022	6.9
Ti I (6)	0.1875	−0.2236	0.1182	−4.8

4. Discussion

In the context of existing measurements of magnetic fields for large samples of cool stars (e.g., Reiners et al. 2009; Afram & Berdyugina 2019; Shulyak et al. 2019), we argue the impact of this work is the empirical detection of saturation of a photospheric signature with Rossby number. Previous efforts in this area have involved complex modeling of spectra to determine magnetic field strengths, however, the conversion from spectra to magnetic field is not straightforward, and the authors are unaware of a clear detection of saturation in equivalent width in absorption with Rossby number for M dwarfs in the literature. As for the physical source of the Zeeman enhancement, it is unclear whether it arises from isolated magnetic spots, a global magnetic field, or a combination of the two.

In combination with the results on FeH lines from Reiners et al. (2009), these results strongly suggest that the saturation mechanism occurs at or below the stellar photosphere and not the chromosphere or corona. That is to say the magnetic fields in the photosphere itself are saturated. However, the fundamental nature of that mechanism remains a mystery. The saturation may well be the fundamental conversion of rotational/convective sheering into a magnetic field in the first place.

4.1. Metallicity

Recently, Passegger et al. (2019) made the important point that using magnetically sensitive lines may corrupt metallicity

determinations unless Zeeman enhancement is modeled. In their work, they determined metallicities of M dwarfs in the CARMENES data using model atmospheres and magnetically insensitive lines. Shulyak et al. (2019) made a similar point, stating that measurements of magnetic field strength using Zeeman enhancement require an estimate of the metallicity. In this work, we side step the issue of measurement metallicity or magnetic fields, instead focusing on the observational evidence for a saturation mechanism at or below the M-dwarf photosphere. However, metallicity may add to the scatter in Figure 4.

Nevertheless, it is important to discuss the implications this work has for metallicity determinations. Veyette et al. (2017) and Veyette & Muirhead (2018) used the same Ti I lines to determine the α enrichment of M-dwarf stars and measure the chemical-kinematic ages of exoplanet hosts without considering magnetic effects. However, Veyette et al. (2017) found that M dwarfs known to have enhanced Ti (based on the Ti content of FGK companions) did in fact show larger Ti equivalent widths and followed the equivalent width-metallicity trends expected from nonmagnetic stellar atmosphere models (see their Figure 4). That is to say, without considering magnetic effects, Veyette et al. (2017) found that equivalent widths of Ti I lines trace Ti abundance. In this work, without considering metallicity effects, we find that equivalent widths of Ti I lines trace magnetic enhancement. Combining these results, it appears that magnetic enhancement is a source of scatter in the metallicity relations, and vice versa: metallicity is a source of scatter in magnetic enhancement. This is entirely empirical: we see these trends without employing any M-dwarf atmospheric models, which are subject to their own peculiar systematic errors.

4.2. Radius Inflation

This work is part of a larger paper series on the nature of discrepancies between modeled and measured radii of M-dwarf stars and what role, if any, magnetic fields play in that discrepancy (Magnetic Inflation and Stellar Mass, Han et al. 2017, 2019; Kesseli et al. 2018; Healy et al. 2019). A prominent theory for the discrepancies involves magnetic inhibition of convection in the outer, super-adiabatic layer of

the star (Chabrier et al. 2007). If the magnetic fields in the photosphere saturate, as implied by our results, it suggests that M dwarfs of similar masses in the saturated regime (Ro $\lesssim$ 0.1) should have the same degree of radius inflation with respect to a fiducial value: either predictions from nonmagnetic evolutionary models or nonactive M dwarfs with high Rossby number.

4.3. Magnetic Variability

We note that magnetic activity indicators are known to change in time as stars rotate and go through their activity cycles. Time-domain observations of activity indicators (including the equivalent widths of magnetically sensitive lines like those analyzed here) will enable a global and cycle-integrated view of M-dwarf surface fields, rather than a snapshot in time. With long-term, high-cadence magnetic spectroscopic monitoring of M-dwarf stars, similar to the Mt. Wilson program to monitor the Ca II H and K lines in nearby Sun-like stars (Wilson 1966), we can further test predictions concerning the role of magnetic activity of M-dwarf radii.

ORCID iDs

Philip S. Muirhead ⓘ https://orcid.org/0000-0002-0638-8822
Mark J. Veyette ⓘ https://orcid.org/0000-0002-0385-2183
Elisabeth R. Newton ⓘ https://orcid.org/0000-0003-4150-841X
Christopher A. Theissen ⓘ https://orcid.org/0000-0002-9807-5435
Andrew W. Mann ⓘ https://orcid.org/0000-0003-3654-1602

References

Afram, N., & Berdyugina, S. V. 2019, A&A, 629, A83
Allard, F., Homeier, D., & Freytag, B. 2012, RSPTA, 370, 2765
Astropy Collaboration, Robitaille, T. P., Tollerud, J. E., et al. 2013, A&A, 558, A33
Basri, G., Marcy, G. W., & Valenti, J. A. 1992, ApJ, 390, 622
Berger, E. 2006, ApJ, 648, 629
Bouvier, J., Matt, S. P., Mohanty, S., et al. 2014, in Protostars and Planets VI, ed. H. Beuther et al. (Tucson, AZ: Univ. Arizona Press), 433
Chabrier, G., Gallardo, J., & Baraffe, I. 2007, A&A, 472, L17
Charbonneau, D., Berta, Z. K., Irwin, J., et al. 2009, Natur, 462, 891
Cushing, M. C., Vacca, W. D., & Rayner, J. T. 2004, PASP, 116, 362
Cutri, R. M., Skrutskie, M. F., van Dyk, S., et al. 2003, 2MASS All Sky Catalog of Point Sources (Washington, DC: NASA)
Díez Alonso, E., Caballero, J. A., Montes, D., et al. 2019, A&A, 621, A126
Dittmann, J. A., Irwin, J. M., Charbonneau, D., et al. 2017, ApJ, 836, 124
Dittmann, J. A., Irwin, J. M., Charbonneau, D., & Newton, E. R. 2016, ApJ, 818, 153
Douglas, S. T., Agüeros, M. A., Covey, K. R., et al. 2014, ApJ, 795, 161
Fowler, A. M., & Gatley, I. 1990, ApJL, 353, L33
France, K., Loyd, R. O. P., Youngblood, A., et al. 2016, ApJ, 820, 89
Gaia Collaboration, Brown, A. G. A., Vallenari, A., et al. 2018, A&A, 616, A1
Han, E., Muirhead, P. S., Swift, J. J., et al. 2017, AJ, 154, 100
Han, E., Muirhead, P. S., & Swift, J. J. 2019, AJ, 158, 111
Healy, B. F., Han, E., Muirhead, P. S., et al. 2019, AJ, 158, 89
Horne, K. 1986, PASP, 98, 609
Jardine, M., & Unruh, Y. C. 1999, A&A, 346, 883
Kay, C., Opher, M., & Kornbleuth, M. 2016, ApJ, 826, 195
Kesseli, A. Y., Muirhead, P. S., Mann, A. W., & Mace, G. 2018, AJ, 155, 225
Kurucz, R. L. 2010, obert L. Kurucz Online Database of Observed and Predicted Atomic Transitions, http://kurucz.harvard.edu/
Levenberg, K. 1944, QApMa, 2, 164
Mann, A. W., Dupuy, T., Kraus, A. L., et al. 2019, ApJ, 871, 63
Mann, A. W., Feiden, G. A., Gaidos, E., Boyajian, T., & von Braun, K. 2015, ApJ, 804, 64
Marquardt, D. W. 1963, SJAM, 11, 431
Martin, E. C., Fitzgerald, M. P., McLean, I. S., et al. 2018, Proc. SPIE, 10702, 107020A
McLean, I. S., Becklin, E. E., Bendiksen, O., et al. 1998, Proc. SPIE, 3354, 566
Muirhead, P. S., Vanderburg, A., Shporer, A., et al. 2013, ApJ, 767, 111
Newton, E. R., Charbonneau, D., Irwin, J., & Mann, A. W. 2015, ApJ, 800, 85
Newton, E. R., Irwin, J., Charbonneau, D., et al. 2017, ApJ, 834, 85
Noyes, R. W., Hartmann, L. W., Baliunas, S. L., Duncan, D. K., & Vaughan, A. H. 1984, ApJ, 279, 763
Pallavicini, R., Golub, L., Rosner, R., et al. 1981, ApJ, 248, 279
Passegger, V. M., Schweitzer, A., Shulyak, D., et al. 2019, A&A, 627, A161
Paulson, D. B., Allred, J. C., Anderson, R. B., et al. 2006, PASP, 118, 227
Piskunov, N. E., Kupka, F., Ryabchikova, T. A., Weiss, W. W., & Jeffery, C. S. 1995, A&AS, 112, 525

Pizzolato, N., Maggio, A., Micela, G., Sciortino, S., & Ventura, P. 2003, A&A, 397, 147

Quirrenbach, A., Amado, P. J., Caballero, J. A., et al. 2016, Proc. SPIE, 9908, 990812

Reiners, A., Basri, G., & Browning, M. 2009, ApJ, 692, 538

Reiners, A., Zechmeister, M., Caballero, J. A., et al. 2018, A&A, 612, A49

Ryabchikova, T., Piskunov, N., Kurucz, R. L., et al. 2015, PhyS, 90, 054005

Savitzky, A., & Golay, M. J. E. 1964, AnaCh, 36, 1627

Schwarz, G. 1978, AnSta, 6, 461

Shulyak, D., Reiners, A., Engeln, A., et al. 2017, NatAs, 1, 0184

Shulyak, D., Reiners, A., Nagel, E., et al. 2019, A&A, 626, A86

Shulyak, D., Reiners, A., Wende, S., et al. 2010, A&A, 523, A37

Skinner, J. N., Thorstensen, J. R., & Lépine, S. 2014, AJ, 148, 115

Skrutskie, M. F., Cutri, R. M., Stiening, R., et al. 2006, AJ, 131, 1163

Soderblom, D. R., Stauffer, J. R., Hudon, J. D., & Jones, B. F. 1993, ApJS, 85, 315

Stelzer, B., Damasso, M., Scholz, A., & Matt, S. P. 2016, MNRAS, 463, 1844

Stewart, R. T., Innis, J. L., Slee, O. B., Nelson, G. J., & Wright, A. E. 1988, AJ, 96, 371

Tran, H. D., Cohen, R., Colson, A., et al. 2016, Proc. SPIE, 9910, 99102E

Veyette, M. J., & Muirhead, P. S. 2018, ApJ, 863, 166

Veyette, M. J., Muirhead, P. S., Mann, A. W., et al. 2017, ApJ, 851, 26

Vilhu, O. 1984, A&A, 133, 117

Wilson, O. C. 1966, ApJ, 144, 695

Winters, J. G., Henry, T. J., Jao, W.-C., et al. 2019, AJ, 157, 216

Winters, J. G., Irwin, J., Newton, E. R., et al. 2018, AJ, 155, 125

Wright, N. J., Drake, J. J., Mamajek, E. E., & Henry, G. W. 2011, ApJ, 743, 48

Wright, N. J., Newton, E. R., Williams, P. K. G., Drake, J. J., & Yadav, R. K. 2018, MNRAS, 479, 2351